Suplemento de la Revista Mexicana de Física **1** (3) 31–35 JULY–AUGUST 2020

Numerical implementation of a Mach-Zehnder interferometer for Bose-Einstein condensates

J. Gil-Londoño, G. Marín-Alvarado, and K. Rodríguez-Ramírez
Departamento de Física, Universidad del Valle, A.A. 25360, Cali, Colombia.
e-mai: karem.c.rodriguez@correounivalle.edu.co

Received 7 September 2019; accepted 29 January 2020

We numerically implement a Mach-Zehnder interferometer, where the coherence and oscillatory properties of Bose-Einstein condensates are explored and the system is modeled by the Gross-Pitaevskii equation. Several time-dependent external trapping potentials were engineered seeking the adiabatic regime which is quantified using fidelity measurements with respect to the actual ground-state of the trap. The dynamics of both conjugate variables, namely density and phase of the matter-wave function, are shown. Moreover, the density and fidelity profiles of the system are presented when the phase-shifter is switching-on and -off, being found in the presented profiles that the system exhibits three different regimes during the recombination stage among them even an orthogonal BEC to the original one is obtained. We achieve the numerical solution through an adequate implementation of the finite-difference method for the spatial discretization and a Runge-Kutta method for the time evolution.

Keywords: Bose-Einstein condensates; atom interferometry; atomic and molecular physics; coherent optical effects.

Se implementa numéricamente un interferómetro Mach-Zehnder, donde se exploran la coherencia y las propiedades oscilatorias de los condensados de Bose-Einstein, el sistema se modela mediante la ecuación de Gross-Pitaevskii. Se diseñaron varios potenciales de atrapamiento externo dependientes del tiempo con el objetivo de encontrar el régimen adiabático que se cuantifica utilizando mediciones de fidelidad con respecto al estado base actual del potencial. Se muestra la dinámica de ambas variables conjugadas, esto es, la densidad y la fase de la función de onda de materia. Además, se muestran los perfiles de densidad y fidelidad del sistema cuando el modificador de fase se activa, encontrándose en los perfiles presentados que el sistema exhibe tres regímenes diferentes durante la etapa de recombinación, entre ellos se obtiene incluso un BEC ortogonal al original. La solución numérica se logra a través de una implementación adecuada del método de diferencias finitas para la discretización espacial y el método de Runge-Kutta para la evolución temporal.

Descriptores: Condensados de Bose-Einstein; interferometría atómica; física atómica y molecular; efectos ópticos coherentes.

PACS: 03.75.-b; 03.75.Dg; 67.85.-d; 02.70.-c

1. Introduction

Ultracold atoms in external optical traps constitute an extraordinary tool for the analysis of coherent matter under extremely well-controlled conditions as highlighted by the achievement of the Bose-Einstein condensation [1] and the "superatom"-properties it exhibits [2]. The field is growing very fast due to the novel possibilities for studies of fundamental quantum-mechanical processes. High research activity has been reported in the last decade including experimental, theoretical and numerical developments [3, 4].

One of the particular interest focuses on the precise manipulation of the quantum-mechanical macroscopic wave function of the Bose-Einstein condensates (BEC) [5]: It has millions of identical atoms in the same quantum state, and it is large enough to be optically imaged [6]. On the other hand, quantum interference constitutes a major challenge for testing quantum-mechanical foundations [7] besides the realization of ultra-precise measurements [8].

The particle-wave duality allows us to analyze the application of matter-wave interferometers from the experimental, theoretical and numerical points of view [9,10]. Furthermore, the development of atom-optics counterparts to beam splitters, phase-shifters and recombiners makes this field a complement to the optical interferometers [11, 12].

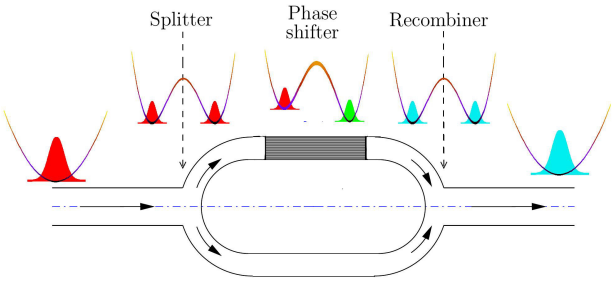

FIGURE 1. Scheme of the implemented Mach-Zehnder interferometer by means of a time-dependent trapping potential described by Eq. (2), see the text.

In this work, we present a numerical implementation of a Mach-Zehnder interferometer (MZI) [13], where the coherence and oscillatory properties of ultracold bosonic matter-waves [14] are explored. The system is modeled by the Gross-Pitaevskii equation (GPE) [15, 16], which is a nonlinear Schödinger equation and is introduced in Sec. 2. The proposed scheme is shown in Fig. 1, and consists of a time-dependent trapping potential which is discussed and described in Sec. 3. The incoming wave is divided into two beams by a $50:50$ beam splitter, one beam travels through a controlled phase-shifter acquiring a phase. Afterwards, the two beams are recombined registering characteristic density

and phase patterns. As presented in Sec. 4, we develop several time-dependent external trapping potentials, and for each case, the fidelity is monitored to analyze the adiabaticity of the dynamical process. Section 5 is devoted to the conclusions and final remarks.

2. Model

We are interested in studying a bosonic cloud in which temperature is very close to the absolute zero, *i.e.* of the order of few micro-Kelvin (μK). Under this circumstance, the system undergoes Bose-Einstein condensation and is described by a macroscopic wave function, $\psi = \psi(\vec{x}, t)$, where the time evolution is determined by the GP equation. After a normalization, introducing a change of variables and providing the effective confinement to be only in one-dimension, the dimensionless Gross-Pitaevskii equation gets as follows [17],

$$i\frac{\partial\psi(x,t)}{\partial t} = \left[-\frac{\epsilon}{2}\nabla^2 + V(x,t) + g|\psi(x,t)|^2\right]\psi(x,t). \quad (1)$$

Here the kinetic energy is measured by $\epsilon = \hbar/(\omega_x m x_s^2) = (a_0/x_s)^2$ where $a_0 = \sqrt{\hbar/\omega_x m}$ is the harmonic-oscillator ground-state length in the $x-$direction, x_s is the characteristic BEC length, and m the atomic mass. We consider the confinement frequencies as $\omega_{y,z} \ll \omega_x$. The interaction strength among the particles is $g = U_0\epsilon^{3/2}$ which is governed by a s-wave contact potential determined by $U_0 = (4\pi a_S N)/(a_0)$, being a_S the s-wave scattering length, and N the number of particles.

The numerical solutions are achieved through an adequate implementation of the finite-differences method for the spatial discretization [18] and the Runge-Kutta method for the time evolution [19]. Hence, the dynamics of both conjugate variables, namely density and phase as well as the fidelity, of the matter-wave function are simulated in this way.

3. BEC time-dependent trapping potential

The BEC is initially trapped in a harmonic potential and an optical lattice is ramped up on time. The resulting time-dependent potential is obtained by a suitable superposition of the form,

$$V(x,t) = \alpha x^2 + \beta(t)\cos^2(\omega x) + \delta(x,t), \quad (2)$$

being $\alpha = 0.85$ half of the constant force.

The ramping up of the optical lattice is a crucial point under the experimental point of view since this process can lead non-adiabiticities that could be end up in an undesired heating of the system [20]. In order to select an adequate beam-splitter, three different ways to rise the lattice are analyzed which are defined as:

$$\beta_1(t) = bt, \quad \beta_2(t) = b\sqrt{1-t_2^2},$$
$$\text{and} \quad \beta_3(t) = b\exp\left(-t_3^2\right), \quad (3)$$

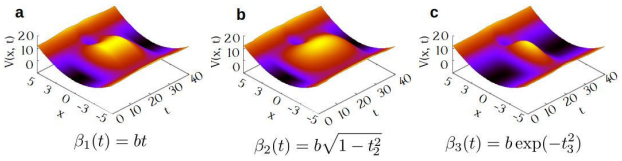

FIGURE 2. As discussed in the text, three different ways to ramp up the optical lattice on time to build the double-well potential out of the initial harmonic confinement are engineered: linear (a), square-root (b) and Gaussian (c).

where $b = 15$ is the strength of the ramping, $t_2 = (t - t_f/2)/b$ in β_2, $t_3 = (t - t_f/2)/(b/3)$ in β_3, and $t_f = 40$ is the final simulation time. The schemes of the potentials generated from the β-functions are presented in Fig. 2, where panel (a) corresponds to the potential generated by $\beta_1(t)$ and panels (b) and (c) to the potentials obtained by $\beta_2(t)$ and $\beta_3(t)$, respectively.

The phase shift in the MZI is carried out by entering the parameter $\delta(x,t)$ in the trapping potential. This parameter is defined in Eq. (4) and allows us to generate a depth difference between the minima of the double-well potential, which translates into a phase difference among the two matter beams,

$$\delta(x,t) = -\delta_0\exp\left[-\frac{(x-x_0)^2}{\sigma_x} - \frac{(t-t_0)^2}{\sigma_t}\right], \quad (4)$$

where $x_0 = 2.530, t_0 = t_f/2 = 20, \sigma_x = 1$, $\sigma_t = 25$ and δ_0 scales the depth of the phase-shifter. The reason for choosing these parameters is because once we set our harmonic confinement, the numerical box is settled as well, therefore, all the potential changes must be performed in such a way that the dimensions of this numerical box are preserved. In particular, the δ-function should be written such that all changes in the trapping potential are clearly separated in the spatial and temporal axes.

The dynamical processes are intended to be in the most adiabatic possible manner. Hence, the particles are prepared in the ground-state of the initial harmonic trap, and then we let the BEC evolves following the potential. To analyze the adiabaticity, we monitored the fidelity ($\mathcal{F}(t)$) by projecting the time-evolved wave-function to the ground state of the external potential at the corresponding time [21],

$$\mathcal{F}(t) = |\langle\psi_{GS}(t)|\psi(t)\rangle|^2. \quad (5)$$

Once we have defined the construction of the confinement potential, we expose in Sec. 4 the dynamics of the implemented Mach-Zehnder interferometer.

4. Interferometer dynamics

We present the density and phase of the matter-wave as a function of time, as well as the fidelity using the designed trapping potentials. In Sec. 4.1, we present the dynamics for the three different activation functions of the optical lattice in order to rise the double-well potential. Furthermore, using

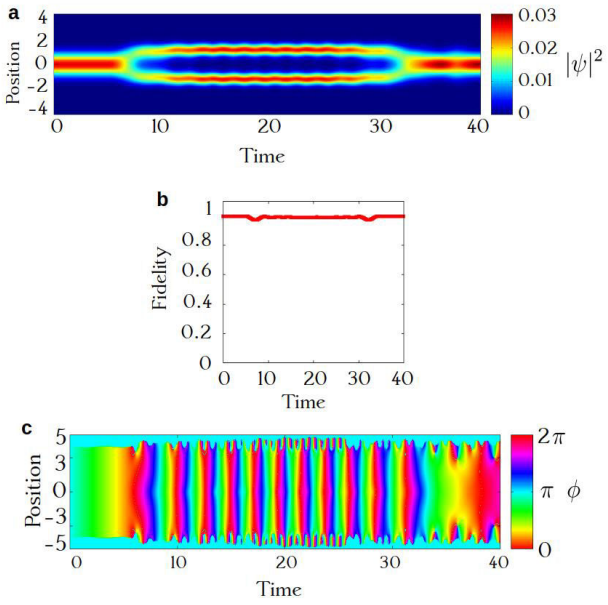

FIGURE 3. Matter-wave interferometer in absence of the phase-shifter, using $\beta_1(t)$, the evolution of the density (a), fidelity (b) and phase (c).

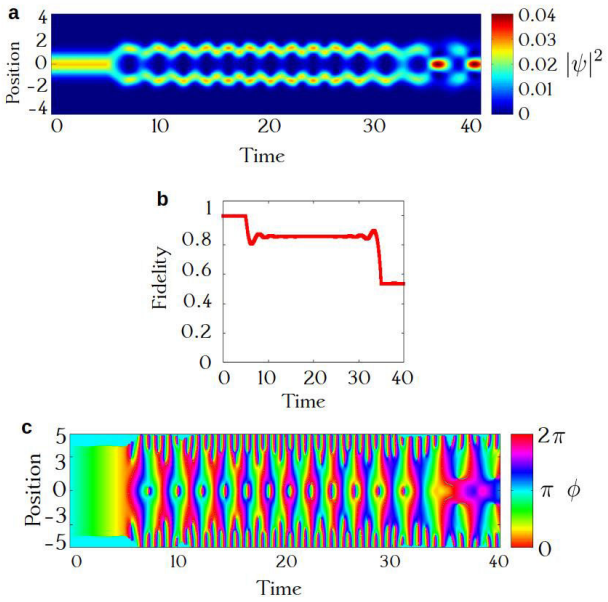

FIGURE 4. Matter-wave interferometer in absence of the phase-shifter, using $\beta_2(t)$, the evolution of the density (a), fidelity (b) and phase (c).

the ramping-time function $\beta_3(t)$ (see Fig. 2(c)), we present in Sec. 4.2, three different regimes resulting in the evolution as a function of the phase-shifter depth.

4.1. Splitting matter-waves

We activate the splitting of matter-waves through the term $\beta(t)$ introduced in Eq. (2). The Figs. 3, 4 and 5 present the obtained dynamics by using the three introduced ramped-up

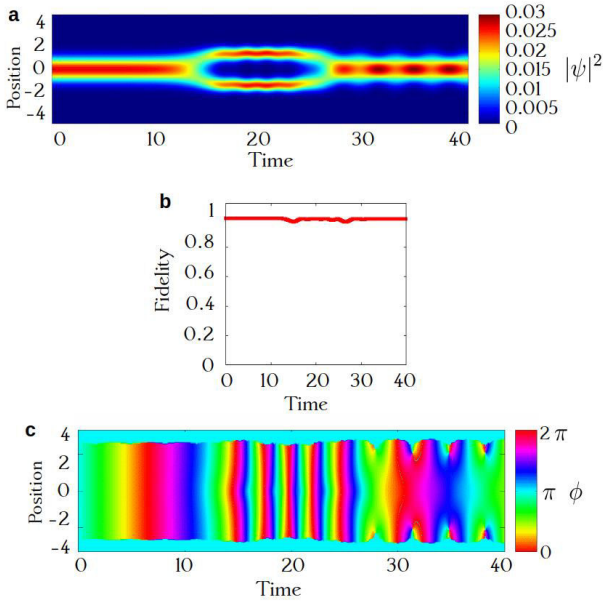

FIGURE 5. Matter-wave interferometer in absence of the phase-shifter, using $\beta_3(t)$, the evolution of the density (a), fidelity (b) and phase (c).

β-functions (see Eq. (3)). Since our purpose is to determine which of the splitters works more properly for our interest the dynamics are initially presented without introducing any phase shifting in the system.

At first, let us start with the dynamics display by using the $\beta_1(t)$ function shown in Fig. 3. In panel 3(a) we observe that the splitted-beams stage lasts longer than the recombination process, being not a good sign for our purposes. The fidelity behavior is presented in panel 3(b), it clearly fits our expectations of having adiabatic evolutions. Indeed, we can see tiny deviations from the unity when the beam-splitter is switching-on and -off. On the other hand, in the phase profile presented in panel 3(c), symmetrical behavior is observed as a function of the position, as expected. Although manifesting edge effects the phase propagates properly.

In the second place, we analyze the matter-wave evolution when the $\beta_2(t)$ function is used as the splitter, see Fig. 4. The density profile presented in panel 4(a) exhibits strong fluctuations, which is evidenced by the strong fall from the unity of the fidelity profile (panel 4(b)), during the splitting and even stronger during the recombination process. Hence, since the evolution of the system moves significantly away from the ground state, even when a phase is not printed in the system, we discard this kind of beam-splitters. The phase profile (panel 4(c)) shows symmetric behavior as a function of the position, however, it presents even stronger undesirable edge effects.

On the other hand, Fig. 5 manifests adequate behavior by using $\beta_3(t)$, that is, the recombination process in the density profile lasts longer as it is observed in panel 5(a); besides, the dynamics of the system is adiabatic enough to fulfill our requirements, which is evidenced in the fidelity profile (see

panel 5(a)). Here, the evolved state presents a small deviation from the ground state only at the times when a change in the confinement potential is introduced but the fidelity returns to one rapidly in the recombination stage. Contrary to the phase profiles illustrated in Figs. 3 and 4, no edge effects are observed at all, as it is shown in panel 5(c). Therefore, in order to study the dynamics developed by the inclusion of the phase-shifter, Eq. (4), in the interferometer, we conclude that the best analyzed beam-splitter is generated by $\beta_3(t)$, hence, all the subsequent results are obtained using it.

4.2. Phase-shifter

Once the initial beam is splitted in two, a phase difference is introduced by the phase-shifter described in Eq. (4).

The term δ_0 in the parameter $\delta(x,t)$, take values between $\delta_0 = 0$ and $\delta_0 = 12.0$, establishing a maximum relative depth between the minima of the double-well potential of $h \approx 5.51$, while the horizontal distance between the wells is $x \approx 3.31$. Figures 6, 7 and 8 show the density and fidelity profiles for different relative depths, and three distinct behaviors can be seen.

Panels (a), (c) and (e) of Fig. 6 present the density profiles for the relative depths generated by $\delta_0 = 2.0$, $\delta_0 = 6.0$ and $\delta_0 = 9.4$ respectively. In these panels, a minimum population in the central position during the recombination stage is evidenced. On the other hand, panels (b), (d) and (f) show the obtained fidelity profiles. Here, a sudden decay in two steps is observed, one in the beam splitting stage and then in the recombination. Clearly showing that the recombined state is orthogonal to the ground-state of the single-well potential, and an identical behavior for these three relative depths is observed.

Figure 7 displays the density profiles (panels (a), (c) and (e)) and the fidelity curves (panels (b), (d) and (f)) introducing potential depths of $\delta_0 = 3.0$, $\delta_0 = 6.8$ and $\delta_0 = 10.2$, respectively. The density profiles show that during the recombination process the maximum distribution of the particles tends to stay in the classical returning points in an alternative manner. Panels (b), (d) and (f) show that the fidelity moves away notoriously from the unit once the potential is modified, although reaching a stable value higher than the one discussed in the previous case. It suggests that the recombined state has at least a tiny probability to be in the ground-state among its superposition.

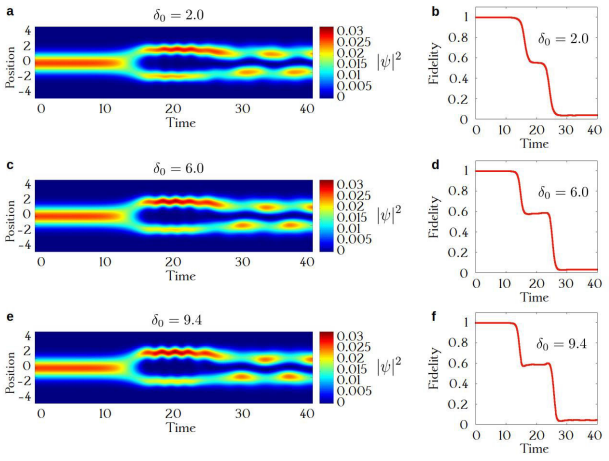

FIGURE 6. Matter-wave interferometer in presence of the phase-shifter, using $\beta_3(t)$, the evolution of the density ((a), (c), (e)) and fidelity ((b), (d), (f)). Regime 1.

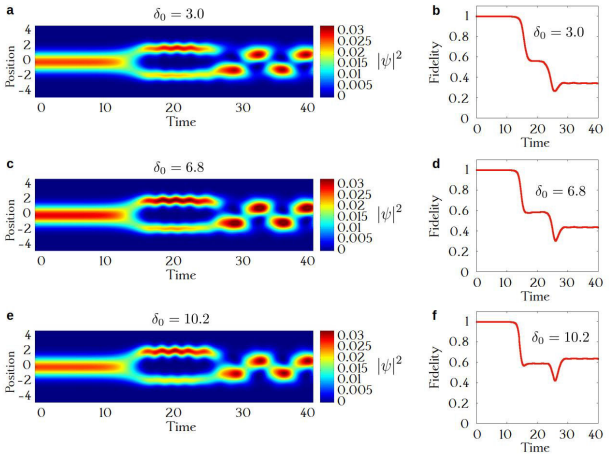

FIGURE 7. Matter-wave interferometer in presence of the phase-shifter, using $\beta_3(t)$, the evolution of the density ((a), (c), (e)) and fidelity ((b), (d), (f)). Regime 2.

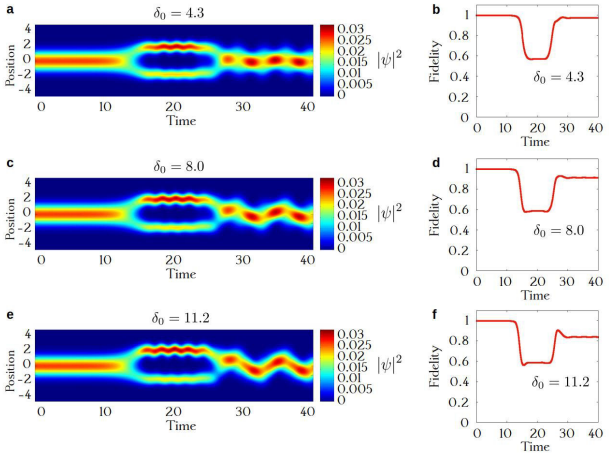

FIGURE 8. Matter-wave interferometer in presence of the phase-shifter, using $\beta_3(t)$, the evolution of the density ((a), (c), (e)) and fidelity ((b), (d), (f)). Regime 3.

Figure 8 exhibits the density profiles for depths of $\delta_0 = 4.3$, $\delta_0 = 8.0$ and $\delta_0 = 11.2$ (panels (a), (c) and (e), respectively), it is observed that the density in the recombination stage oscillates around the central position. On the other hand, panels (b), (d) and (f) show the corresponding fidelity profiles and it can be seen deviations from the unit during the beam splitting process but it recovers, although not completely but still good enough in the recombination stage.

In summary, three specific regimes have been manifested in the dynamics of the implemented interferometer.

5. Conclusions

We build numerically a time-dependent external trapping potential to confine Bose-Einstein condensates and simulate a Mach-Zehnder interferometer. In order to do so, three activation functions of the double-well potential were considered and, based on the set of defined observables, the $\beta_3(t)$ function has been chosen to lead to the most adiabatic possible dynamics. This function takes the important role of the matter-wave beam-splitter for our interferometer.

Once the beam-splitter is established, the phase-shifter $\delta(x,t)$ is introduced in the confinement potential, through which a relative depth was generated between the minima of the double-well potential. $\delta(x,t)$ had a range of variation mediated by parameter δ_0, which generates relative depth values between $h=0$ and $h\approx 5.51$, while the distance between the wells is kept at $x\approx 3.31$.

It was found that the dynamics of the system exhibits three distinct regimes in the recombination stage, which must be analyzed in detail in future works.

1. M. H. Anderson, J. R. Ensher, M. R. Matthews, C. E. Wieman, and E. A. Cornell, *Sci.* **269** (1995) 198.
2. K. B. Davis *et al., Phys. Rev. Lett.* **75** (1995) 3969.
3. I. Bloch, J. Dalibard, and W. Zwerger, *Rev. Mod. Phys*. **80** (2008) 885.
4. S. Giorgini, L. P. Pitaevskii, and S. Stringari, *Rev. Mod. Phys.* **80** (2008) 1215.
5. R. Corgier *et al., New J. Phys.* **20** (2018) 055002.
6. F. V. Pepe, *Bose-einstein condensation: static and dynamical aspects*, Ph.D. thesis, Universit Degli Studi Di Bari Aldo Moro (2013).
7. T. van Zoest *et al., Sci.* **328** (2010) 1540.
8. A. O. Jamison, *Precision interferometry with bose-einstein condensates*, Ph.D. thesis, University of Washington (2014).
9. T. Schumm *et al., Nat. Phys*. **1** (2005) 57.
10. S. van Frank *et al., Nat. Commun.* **5** (2014) 4009.
11. A. D. Cronin, J. Schmiedmayer, and D. E. Pritchard, *Rev. Mod. Phys*. **81** (2009) 1051.
12. T. Berrada, S. van Frank, R. Bücker, T. Schumm, J.-F. Schaff, and J. Schmiedmayer, *Nat. Commun.* **4** (2013) 2077.
13. G. D. McDonald *et al., Phys. Rev. A* **87** (2013) 013632.
14. B. Lücke *et al., Sci.* **334** (2011) 773.
15. E. P. Gross, *II Nuovo Cimento* (1955-1965) **20** (1961) 454.
16. L. Pitaevskii, *Sov. Phys. JETP* **13** (1961) 451.
17. W. Bao, D. Jaksch, and P. A. Markowich, *J. Comput. Phys.* **187** (2003) 318.
18. W. C. David Kincaid, *Numerical Analysis: Mathematics of Scientific Computing*, 3rd ed. (American Mathematical Society, Providence Rhode Island, 2009), pages 589-593.
19. A. D. S. R. Kent Nagle, Edward B. Saff, *Ecuaciones Diferenciales y Problemas con Valores en la Frontera*, 4 ed. (Pearson Educación, México, 2009), págs. 135-137.
20. M. Dolfi, A. Kantian, B. Bauer, and M. Troyer, *Phys. Rev. A* **91** (2015) 033407.
21. O. Lychkovskiy, O. Gamayun, and V. Cheianov, *Phys. Rev. B* **98** (2018) 024307.